

Subharmonic oscillations in the Floquet circuit with the frequency-synthesis dimension

Bo Lv^{1*}, Shiyun Xia¹, Ye Tian², Ting Liu³, Hongyang Mu¹, Zhichao Shen¹, Sijie Wang¹, Zheng Zhu¹, Huibin Tao⁴, Fanyi Meng^{5*}, Jinhui Shi^{1*}

¹Key Laboratory of In-Fiber Integrated Optics of Ministry of Education, College of Physics and Optoelectronic Engineering, Harbin Engineering University, Harbin 150001, Heilongjiang Province, China

²College of Automation, Nanjing University of Science and Technology, Nanjing 210000, Jiangsu Province, China

³College of Underwater Acoustic Engineering, Harbin Engineering University, Harbin 150001, China

⁴School of Software Engineering, Xi'an Jiaotong University, Xi'an, China

⁵Department of microwave engineering, school of electronics and information, Harbin Institute of Technology, Harbin 150001, Heilongjiang Province, China

*Correspondence to:

bolv@hrbeu.edu.cn, blade@hit.edu.cn, shijinhui@hrbeu.edu.cn.

Abstract

The period-doubling oscillation emerges with the coexistence between zero and π modes in Floquet topological insulator. Here, utilizing the flexibility of the circuit, we construct the Floquet circuit with frequency-synthetic dimension and find the topological-protected deeply-subharmonic oscillations with the period extensively exceeding the doubling-driven period. In the construction framework, the periodically-driven mechanism is attained by implementing the circuit-oscillator hierarchy with the stepping-variation resonances in frequency domain. The zero and π modes that arise at the Floquet band in the circuit indicate the anomalous boundary-bulk correspondence. The coexistence of zero and π modes, results in a subharmonic oscillation with the extremely-low frequency on the edge of the Floquet circuit. Furthermore, we explore the Floquet band with the enhanced periodically-driven strength tailored by the component flexibility of the circuit. Our method provides a flexible scheme to study

Floquet topological phases, and open a new path for realizing the deeply subwavelength system.

Key words: Floquet circuit, Floquet topological phases, deeply-subharmonic oscillation, frequency-synthesis dimension.

Introduction

In recent years, topological insulators (TIs) have attracted numerous investigation due to their unique physical properties [1-5]. Within this domain, Floquet topological insulators (FTIs), characterized by their response to periodic modulation [6-10], exhibit many distinctive topological phenomena, including the topological π modes [11-12], double-periodic resonance [13-14], the Floquet-Majorana states [15-18] and combining the non-Hermitian system [19], quantum Hall conductor [20, 21], high-dimensional [22-27] and high-order topological insulators [28-37]. Various theoretical and experimental platforms have been proposed for realization of FTIs. In the realm of condensed matter physics, the investigations into Floquet topological phases have been conducted using ultracold atom lattices [38], superconductors [40-50] and semiconductor quantum wells [51]. Meanwhile, in the context of classical physics, Floquet topological phases have been realized within optical [52-57] and acoustic systems [58-59], demonstrating the broad applicability and interdisciplinary interest in these driven steady states of matter.

Due to the challenges associated with the realization of time regulation in condensed matter, optical and acoustic systems, researchers have tuned to alternative methods to realize FTIs. The mechanism of periodic modulation is achieved by constructing helicity waveguide or employing periodically varied-spatial dimension [6, 11, 13, 59]. However, these approaches are subject to spatial-geometrical constraints, which complicate assembly and the range of modulable-frequencies. Among classical physical systems, electric circuits with their highly flexible-integration performance, is serve as suitable platforms of FTIs [60-64]. Here, periodic modulation can be implemented through the use of active elements or spatial modulation [65-67].

In this study, a Floquet circuit is designed to achieve Floquet topological phases. The architecture of the circuit incorporates a chain in each row, braided according to the Su-Schrieffer-Heeger (SSH) model. This configuration is constructed using on-site resonators, grounded in-parallel inductors and capacitors, and incorporating hopping terms through intralayer-coupling capacitors. Adjacent rows of resonators are interconnected via interlayer-coupling capacitors. Periodic modulation within this system is facilitated by the introduction of a frequency-synthetic dimension, achieved by systematically varying the on-site resonant frequencies along different rows. When the difference in resonant frequency between adjacent rows decreases below the static band of the SSH circuit chain, topological π modes manifest within the Floquet band. Subsequent adjustment of the intralayer-coupling capacitors' values leads to the emergence of zero modes. The coexistence of π and zero modes induces deeply subharmonic oscillation at the edge of the circuit. Furthermore, we explore the Floquet band behavior under conditions of significant time-modulation amplitude. The developed Floquet circuit holds potentials for applications in generating very low frequency (VLF) signal, which are crucial for underwater communication and seabed detection, and moreover, it provides a novel method for achieving deeply long-wavelength resonance in various systems.

The construction of the Floquet circuit

The Hamiltonian with time-periodic evolution $H(t + T) = H(t)$ in momentum space reads [65]:

$$H(k, t) = \begin{pmatrix} 0 & t_a(t) + t_b(t)e^{-ik} \\ t_a(t) + t_b(t)e^{ik} & 0 \end{pmatrix} \quad (1)$$

where the coupling parameters are $t_{a,b} = t_{a,b} + 2V \cos(\Omega t)$ with the driven frequency $\Omega = \frac{2\pi}{T}$. The eigenvalues of the Hamiltonian in Eq. 1 are corresponding to the resonant frequencies of the classical circuit. Thus, the Planck constant is set to 1. The time-dependent dynamic equation has the form as

$$(H(k, t) - i\partial_t)|\psi(t)\rangle = 0, \quad (2)$$

According to the Floquet theory, the Floquet Hamiltonian is defined as $H_F = H(k, t) - i\partial_t$, and the Floquet state can be expressed as $|\psi(t)\rangle = \exp(-i\varepsilon t)|\varphi(t)\rangle$, where ε and $|\varphi(t)\rangle$ are the quasienergy and time-periodic mode. The eigen equation of H_F can be expressed as $H_F|\varphi(t)\rangle = \varepsilon|\varphi(t)\rangle$. Next, the Floquet states are expanded with Fourier series for getting rid of the time-dependent part. The Fourier expansion of the Floquet state at the quasienergy ε_n has the form

$$|\psi_n(t)\rangle = \exp(-i\varepsilon_n t) \sum_m \exp(-im\Omega t) |\phi_n^{(m)}\rangle, \quad (3)$$

where $|\phi_n^{(m)}\rangle$ is the m th Fourier component of $|\varphi_n(t)\rangle$. Through the above Fourier transform, the states $|\psi(t)\rangle$ are expanded in the space $S = T' \otimes F$, in which T' is the Hilbert space with the complete and orthonormal basis $\{|\varphi_n(t)\rangle\}$, and F is the Fourier space with the basis $\{\exp(-im\Omega t) |\phi_n^{(m)}\rangle\}$ with integer m presenting the Fourier order. In the Fourier space, the equation of the quasienergy ε_n reads:

$$\sum_{m'} H_{mm'} |\phi_n^{(m')}\rangle = \varepsilon_n |\phi_n^{(m)}\rangle \quad (4)$$

where $H_{mm'} = m\Omega\delta_{mm'}I + H_{m-m'}$, in which $H_{m-m'}$ is the Fourier component of the time-dependent Hamiltonian $H(t)$ and has the form $H_l = \frac{1}{T} \int_0^T \exp(-il\Omega t) H(t) dt$ with the index $l = m - m'$. The matrix of the Floquet Hamiltonian H_F can be expressed as the form

$$H_F = \begin{pmatrix} \ddots & \vdots & \vdots & \vdots & \vdots & \vdots & \ddots \\ \cdots & H_0 - 2\Omega & H_{-1} & 0 & 0 & 0 & \cdots \\ \cdots & H_1 & H_0 - \Omega & H_{-1} & 0 & 0 & \cdots \\ \cdots & 0 & H_1 & H_0 & H_{-1} & 0 & \cdots \\ \cdots & 0 & 0 & H_1 & H_0 + \Omega & H_{-1} & \cdots \\ \cdots & 0 & 0 & 0 & H_1 & H_0 + 2\Omega & \cdots \\ \ddots & \vdots & \vdots & \vdots & \vdots & \vdots & \ddots \end{pmatrix} \quad (5)$$

The Fourier components of the Hamiltonian in Eq. 1 have the forms

$$H_0 = \begin{pmatrix} 0 & t_a + t_b e^{-ik} \\ t_a + t_b e^{ik} & 0 \end{pmatrix}, \quad (6)$$

$$H_1 = H_{-1} = \begin{pmatrix} 0 & V(1 + e^{-ik}) \\ V(1 + e^{ik}) & 0 \end{pmatrix}, \quad (7)$$

and $H_l = 0$ for $l \geq 2$. The matrix of the Floquet Hamiltonian is expressed as

$$H_F = \begin{pmatrix} \ddots & \vdots & \vdots & \vdots & \vdots & \vdots & \vdots & \ddots \\ \cdots & -\Omega & t_a + t_b e^{-ik} & 0 & V(1 + e^{ik}) & 0 & 0 & \cdots \\ \cdots & t_a + t_b e^{ik} & -\Omega & V(1 + e^{ik}) & 0 & 0 & 0 & \cdots \\ \cdots & 0 & V(1 + e^{-ik}) & 0 & t_a + t_b e^{-ik} & 0 & V(1 + e^{ik}) & \cdots \\ \cdots & V(1 + e^{ik}) & 0 & t_a + t_b e^{ik} & 0 & V(1 + e^{ik}) & 0 & \cdots \\ \cdots & 0 & 0 & 0 & V(1 + e^{ik}) & \Omega & t_a + t_b e^{-ik} & \cdots \\ \cdots & 0 & 0 & V(1 + e^{ik}) & 0 & t_a + t_b e^{ik} & \Omega & \cdots \\ \vdots & \vdots & \vdots & \vdots & \vdots & \cdots & \vdots & \ddots \end{pmatrix} \quad (8)$$

Mimic the schematic of the Floquet Hamiltonian, the Floquet circuit is constructed as shown in Fig. 1a, and the components of the model are listed in Fig. 1b. The label of the row is indicated as the order m ($\{m|m \in [-M, M] \text{ and } m \in \mathbb{Z}\}$), and total number of the row is $2M + 1$. The circuit chain in each row is designed as the SSH model with the on-site section consisting of the grounded-parallel inductor L and capacitor C_m (named as grounded- LC_m resonator) and the intralayer-hopping term consisting of the coupling capacitors C_a and C_b . The values of the grounded capacitors in different rows present stepped variation as $C_{m+1} - C_m = C_\Omega$, and the nodes between the nearest-neighbor rows are staggered connected by the interlayer-capacitor C_v . We set the voltages on the circuit nodes with the frequency ω . The circuit model with the infinite boundary along the rows and the maximum order is $M = 2$. According to the Kirchhoff law, the dynamic equation of the Floquet circuit is calculated as [60-64]

$$\frac{\omega_0^2}{\omega^2} V = HV \quad (9)$$

where $\omega_0 = \frac{1}{\sqrt{LC_0}}$ in which the capacitor C_0 is corresponding to the grounded capacitor in the row of the order $m = 0$. The effective Hamiltonian H of the Floquet circuit in Eq. 9 possess the form as

$H(k) =$

$$\begin{pmatrix} 1+t-2t_\Omega & -t_a-t_b e^{-ik} & 0 & -t_v(1+e^{-ik}) & 0 & 0 & 0 & 0 & 0 & 0 \\ -t_a-t_b e^{ik} & 1+t-2t_\Omega & -t_v(1+e^{ik}) & 0 & 0 & 0 & 0 & 0 & 0 & 0 \\ 0 & -t_v(1+e^{-ik}) & 1+t-t_\Omega & -t_a-t_b e^{-ik} & 0 & -t_v(1+e^{-ik}) & 0 & 0 & 0 & 0 \\ -t_v(1+e^{ik}) & 0 & -t_a-t_b e^{ik} & 1+t-t_\Omega & -t_v(1+e^{ik}) & 0 & 0 & 0 & 0 & 0 \\ 0 & 0 & 0 & -t_v(1+e^{-ik}) & 1+t & -t_a-t_b e^{-ik} & 0 & -t_v(1+e^{-ik}) & 0 & 0 \\ 0 & 0 & -t_v(1+e^{ik}) & 0 & -t_a-t_b e^{ik} & 1+t & -t_v(1+e^{ik}) & 0 & 0 & 0 \\ 0 & 0 & 0 & 0 & 0 & -t_v(1+e^{-ik}) & 1+t+t_\Omega & -t_a-t_b e^{-ik} & 0 & -t_v(1+e^{-ik}) \\ 0 & 0 & 0 & 0 & -t_v(1+e^{ik}) & 0 & -t_a-t_b e^{ik} & 1+t+t_\Omega & -t_v(1+e^{ik}) & 0 \\ 0 & 0 & 0 & 0 & 0 & 0 & 0 & -t_v(1+e^{-ik}) & 1+t+2t_\Omega & -t_a-t_b e^{-ik} \\ 0 & 0 & 0 & 0 & 0 & 0 & -t_v(1+e^{ik}) & 0 & -t_a-t_b e^{ik} & 1+t+2t_\Omega \end{pmatrix} \quad (10)$$

where the parameters are $t_\Omega = \frac{C_\Omega}{C_0}$, $t_v = \frac{C_v}{C_0}$ and $t_{a/b} = \frac{C_{a/b}}{C_0}$. The eigenvalues of the Hamiltonian in Eq. 10 are corresponding to the square of the normalized-resonant frequencies of the circuit as $\frac{\omega_0^2}{\omega^2}$. Comparing with the form of the Floquet Hamiltonian

in Eq. 8, the element parameters present the correspondence relations as $t_\Omega \leftrightarrow \Omega$, $t_v \leftrightarrow V$ (V presents the amplitude of driven frequency of the time modulation here, and indicates the voltage of the circuit in the following content), and the intralayer-coupling parameters of the two Hamiltonians has the same labels $t_{a/b}$. Here the parameters t_Ω , t_v in Eq. 10 are named as the Driven Frequency (DF) capacitor and the Amplitude of the Periodic Modulation (APM) capacitor. The intralayer coupling capacitor, DF capacitor and APM capacitor in the following content refer to the real capacitors $C_{a/b}$, C_Ω , C_v or the normalized capacitors $t_{a/b}$, t_Ω , t_v . The on-site terms of the Hamiltonian are $t_{on} = 1 + t_a + t_b + 4t_v + mt_\Omega$, which present the step variation trend along different rows as the diagonal terms of the Floquet Hamiltonian in Eq. 8. The circuit model inserts the periodic-time modulation by constructing the frequency-synthetic dimension, which is carried out by setting the step-variation values of the on-site grounded capacitors on different rows which lead the step frequencies of the grounded- LC resonators along the columns. The equivalent method is also proposed in other platforms [65, 68-69]. Specially, the form of the eigenvalue in Eq. 9 indicates that the step-variation term of the Floquet Hamiltonian is corresponding to the difference of the square reciprocal of frequency in the Floquet circuit. Although the on-site energies of the Floquet Hamiltonian in Eq. 8 possess the negative values, the diagonal on-site terms of the effective Hamiltonian of the circuit in Eq. 10 hold the reference frequency $1 + t$ being far greater than the difference t_Ω of the step variation. This mechanism guarantees the eigenvalues of the effective Hamiltonian of the circuit in Eq. 10 hold the positive values.

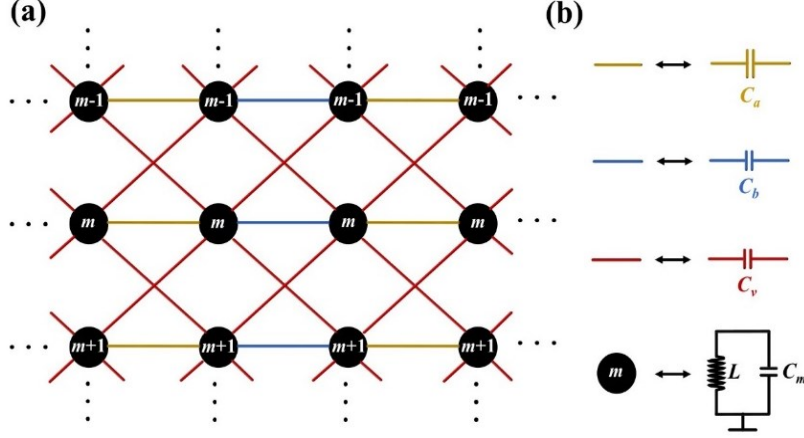


Figure 1. The schematic diagram of the Floquet circuit. **a**, the structure of the electric elements. In each row, the circuit is constructed as the SSH chain, the nodes are staggered coupling between the nearest-neighbor rows indicated by the orders $\{m|m \in [-M, M] \text{ and } m \in \mathbb{Z}\}$. **b**, the element list of the circuit. The components in each row contain the intra- and inter-coupling C_a and C_b , and the grounded inductor and capacitor L and C_m . The interlayer capacitor C_v connects the $a(b)$ nodes to the $b(a)$ nodes in adjacent rows along columns. The lattice in each row contains two nodes with the intra-coupling capacitor C_a , and the hopping term between the lattice is the inter-coupling capacitor C_b .

The π and zero modes in the Floquet topological circuit

When the APM capacitor is zero, the Hamiltonian of the circuit in Eq. 10 is similar to the static Hamiltonian. The width of the band is $W = 2(t_a + t_b)$. Considering nonzero APM capacitor, the form of the effective Hamiltonian in Eq. 10 manifests that the static band is expanded by the Fourier-order multiple of the DF capacitor mt_Ω with the “on-site” and “coupling” terms as $H_0 \pm mt_\Omega$ and $H_{\pm 1}$. The Floquet spectrum can be regard as the effective-particle band with the energy mt_Ω and the local energy is H_0 . The secondary-diagonal terms $H_{\pm 1}$ correspond to the effective-particle scattering between the interlayer bands m and $m + 1$, where the sign “-” implies the emission and absorption processes. All the high-order effective-particle scattering is absent due to the effective-time modulation with single tone t_Ω [13].

Considering the circuit with infinite boundary, using the Bloch theorem, the band

of the effective Hamiltonian in Eq. 10 is calculated as the Fig. 2a-2c. The bands with different orders are indicated by the background colors. When the DF capacitor t_Ω is higher than W , the band gaps between the bands of different orders (we named them as the inter-band gaps. Correspondingly, the band gaps in the bands of each order are named as intra-band gaps) is approximately $t_\Omega - W$, as shown in Fig. 2a. When t_Ω equal to W , the frequency degeneracies arise between the bands with the orders $m = 0$ and ± 1 (the bands in yellow- and green-background regions), as shown in Fig. 2b. The intra-band gaps with $m = \pm 1$ and ± 2 (the bands in green- and blue-background regions) still open because of the hopping terms $H_{\pm 1}$. If the APM capacitor t_v is changed as much less than the intralayer coupling capacitor t_a/t_b , the frequency intervals of the adjacent bands are approximately equal to $|t_\Omega - W|$, and the all the inter-band gaps approach to zero. Comparatively, when the APM capacitor increases to the intralayer-coupling capacitors as $t_v \rightarrow t_a(t_b)$, some inter-band gaps still open (the detail analysis is illustrated in the Section 1 in Appendix). When t_Ω is lower than W , the closed inter-band gaps reopen as Fig. 2c. Above the analysis, the open-close-open process of the inter-band gaps with the gradual change of the DF capacitors reveal the existence of the topological-phase transition at the condition of $t_\Omega \approx W$.

Next, considering the circuit with open boundary and number of the lattice 10 in each row, the effective Hamiltonian in Eq. 10 converts to the real-space form. The spectrum of the Hamiltonian with different values of the DF capacitors are shown in Fig. 2d-2f. The eigen values are all located at the k -space bands when $t_v > W$, as shown in Fig. 2d. Under the condition of $t_v = W$, the eigen values locating at the bands of the orders $m = 0$ and ± 1 are attached as the band degeneracy, as shown in Fig. 2e. When $t_v < W$, some additional-eigen values emerge in the inter-band gaps, as in Fig. 2f. Due to the topological characteristics of the SSH circuit in each row only possessing the non-topological phase under the condition of $t_a > t_b$, the eigen values in the inter-band gaps is generated by adding the frequency-synthetic dimension. From the analysis of the effective Hamiltonian in time domain, these states are the π modes and present nontrivial-topological phase (the analysis in time domain and the topological performance of these modes is illustrated in the Section 2 in Appendix). After that, we

analysis the Floquet band when $t_a < t_b$. The Floquet bands unchanged under this condition as the Fig. 2d-2f. The eigen values emerge in the intra-band gaps regardless of the relation of the driven capacitor C_Ω and the bandwidth of one SSH chain W , as shown in Fig. 2j-2l. The eigen values in the intra-band gaps also present the edge-bulk correspondence which is illustrated in the Section 3 in Appendix. The new type of the eigen values corresponds to the topological-zero mode.

When the values of the intra-layer coupling capacitors are exchanged, the eigen values of zero mode arises at the intra-band gaps, as shown in Fig. 3a. Here the zero-mode quasienergy located at the band of the order $m = 0$ is indicated as $\varepsilon_0^{(0)}$, the values of the zero-mode quasienergy at the bands of other orders are $\varepsilon_0^{(m)} = \varepsilon_0^{(0)} + m\Omega$ with $\{m|m \in [-M, M], M = 2 \text{ and } m \in \mathbb{Z}\}$. Due to the nontrivial-topological performance of the π and zero modes, the states of π and zero modes $\phi_\pi^{(m \leftrightarrow m+1)}$ with $m \in [-M, M - 1]$ and $\phi_0^{(m)}$ with $m \in [-M, M]$ also present the topological bulk-edge correspondence, which is shown in Fig. 3b-3c. Comparing the spatial distribution of the π - and zero-mode states on rows with the quasienergy of different orders, the rows of the circuit from 1st to 5th (from the top row to bottom row) correspond to the orders $m = -2$ to 2. Thus, the rows also be indicated by the order numbers in following content.

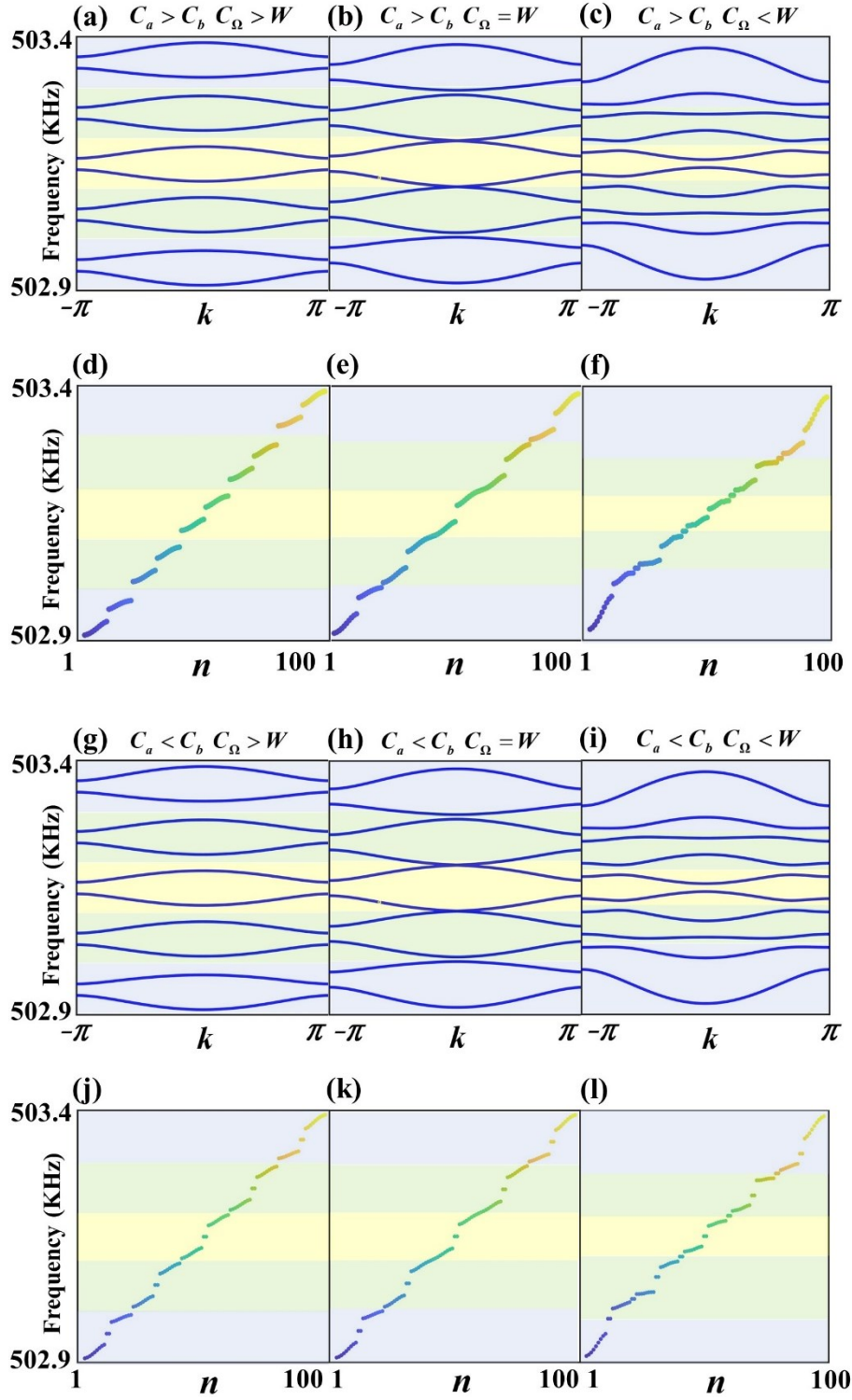


Figure 2. The band and spectrum of the Floquet circuit with different DF capacitors. The values of other electric elements are set as $L = 100$ nH, $C_0 = 1$ μ F and $C_v = 60$ pF. **a-c**, the band of the Floquet Hamiltonian with infinite boundary in Horizontal direction and five rows in the vertical direction when the DF capacitors are set as $C_\Omega = 440$ pF, 400 pF, 260 pF and the intra-coupling capacitors are $C_a = 150$ pF and $C_b = 50$ pF. **d-f**, the spectrum of the Floquet Hamiltonian with open boundary along the

Horizontal direction and the number of the lattice in each row is 10 when the DF capacitors is set as $C_\Omega = 440$ pF, 400 pF and 260 pF. **g-i**, the band of the Floquet Hamiltonian with infinite boundary in Horizontal direction and five rows in the vertical direction when the intra-coupling capacitors are $C_a = 50$ pF and $C_b = 150$ pF. **j-l**, the spectrum of the Floquet Hamiltonian with open boundary along the Horizontal direction when the intra-coupling capacitors are $C_a = 50$ pF and $C_b = 150$ pF. The band and spectrum of different-Fourier orders are indicated by different-color domains (the blue/green/yellow domains are corresponding to the order $m = \pm 2/\pm 1/0$). Here n represents index of the eigen values of the Floquet Hamiltonian with open boundary.

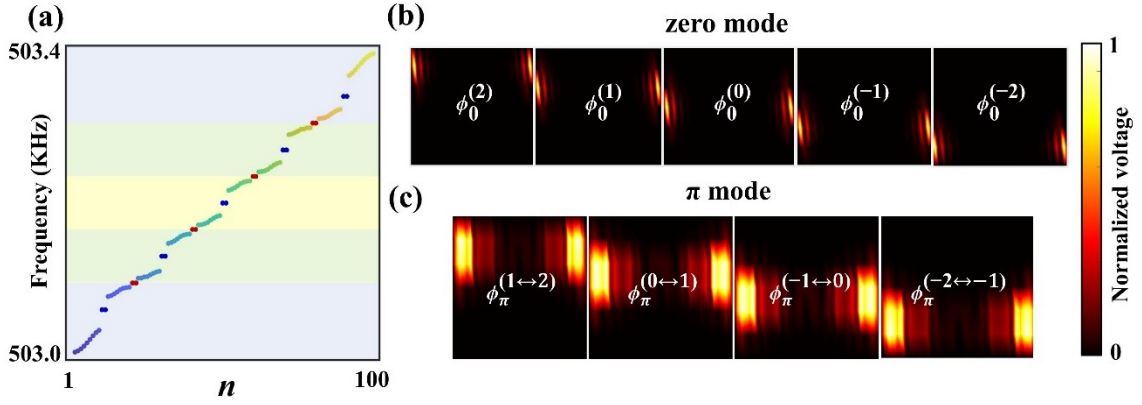


Figure 3. The spectrum under the coexistence of the zero and π mode and the spatial distribution of the zero- and π -mode states. **a**, the spectrum of the Floquet Hamiltonian with open boundary and the number of the lattice is 10. The red and blue points in the inter-band gaps and intra-band gaps are the eigen values of π modes and zero modes. **b/c**, the energy distribution of the zero- and π -modes states. The labels $\phi_0^{(m)}$ and $\phi_\pi^{(m \leftrightarrow m')}$ indicate the zero-mode eigen states at the intra-band gap of the band of the order m and the π -mode eigen states at the inter-band gaps between the bands of the orders m and m' . The intra-layer coupling capacitors are set as $C_a = 50$ pF, $C_b = 150$ pF, $C_\Omega = 260$ pF and the values of the other electric elements are unchanged.

The double-periodic resonance in the Floquet Hamiltonian

Under the condition of the coexistence of zero and π modes, the double-periodic

resonance can be excited at the edge nodes [13, 14]. When the model of the Floquet Hamiltonian is inspired by the signal on the edge node at the m th row, the response signal on the edge node of the m th row is the approximately superposition of the zero and π modes as

$$|\psi(t)\rangle = \gamma_0 e^{-i\varepsilon_0^{(m)}t} \left| \phi_0^{(m)}(t) \right\rangle + \alpha_\pi e^{-i\varepsilon_\pi^{(m-1\leftrightarrow m)}t} \left| \phi_\pi^{(m-1\leftrightarrow m)}(t) \right\rangle + \beta_\pi e^{-i\varepsilon_\pi^{(m\leftrightarrow m+1)}t} \left| \phi_\pi^{(m\leftrightarrow m+1)}(t) \right\rangle \quad (11)$$

where γ_0 , α_π and β_π are the coefficients of the zero mode $\phi_0^{(m)}(t)$ and π modes $\phi_\pi^{(m-1\leftrightarrow m)}(t)$ and $\phi_\pi^{(m\leftrightarrow m+1)}(t)$. When the order is $m = -M$ or M , the coefficients α_π or β_π is zero due to the edge sites of the two rows possessing only one topological π mode $\left| \phi_\pi^{(M-1\leftrightarrow M)} \right\rangle$ or $\left| \phi_\pi^{(-M\leftrightarrow -M+1)} \right\rangle$.

The intensity of the response states can be calculated as

$$\begin{aligned} \Psi(t) = & \gamma_0^2 \left\langle \phi_0^{(m)}(t) \left| \phi_0^{(m)}(t) \right\rangle + \alpha_\pi^2 \left\langle \phi_\pi^{(m-1\leftrightarrow m)}(t) \left| \phi_\pi^{(m-1\leftrightarrow m)}(t) \right\rangle + \right. \\ & \beta_\pi^2 \left\langle \phi_\pi^{(m\leftrightarrow m+1)}(t) \left| \phi_\pi^{(m\leftrightarrow m+1)}(t) \right\rangle + \right. \\ & [\gamma_0 \alpha_\pi e^{-i(\varepsilon_\pi^{(m-1\leftrightarrow m)} - \varepsilon_0^{(m)})t} \left\langle \phi_0^{(m)}(t) \left| \phi_\pi^{(m-1\leftrightarrow m)}(t) \right\rangle + \right. \\ & \gamma_0 \beta_\pi e^{-i(\varepsilon_\pi^{(m\leftrightarrow m+1)} - \varepsilon_0^{(m)})t} \left\langle \phi_0^{(m)}(t) \left| \phi_\pi^{(m\leftrightarrow m+1)}(t) \right\rangle + \right. \\ & \left. \alpha_\pi \beta_\pi e^{-i(\varepsilon_\pi^{(m\leftrightarrow m+1)} - \varepsilon_\pi^{(m-1\leftrightarrow m)})t} \left\langle \phi_\pi^{(m-1\leftrightarrow m)}(t) \left| \phi_\pi^{(m\leftrightarrow m+1)}(t) \right\rangle + H.c.] \quad (12) \end{aligned}$$

From the band of the Floquet Hamiltonian, the intervals between the centers of the bands with adjacent orders are approximately the DF capacitor t_Ω . The quasienergy parameters of the dynamic phases in Eq. 12 are $\left| \varepsilon_\pi^{(m-1\leftrightarrow m)} - \varepsilon_0^{(m)} \right| \approx \left| \varepsilon_\pi^{(m\leftrightarrow m+1)} - \varepsilon_0^{(m)} \right| \approx \frac{t_\Omega}{2}$ and $\left| \varepsilon_\pi^{(m-1\leftrightarrow m)} - \varepsilon_\pi^{(m\leftrightarrow m+1)} \right| \approx t_\Omega$. Under the coexistence of the zero and π mode, the response signals on the edge nodes possess double-periodic resonances with the frequency $\frac{t_\Omega}{2}$. When the values of the intra-layer coupling capacitors t_a and t_b are exchanged, only the π modes exist on the edge nodes. Under this condition, the intensity on the edge nodes of the rows with the orders $m \in [-1, 0, 1]$ only has the dynamic phase $\left| \varepsilon_\pi^{(m-1\leftrightarrow m)} - \varepsilon_\pi^{(m\leftrightarrow m+1)} \right| \approx t_\Omega$, which indicates that the response

signals on these edge nodes only has the resonances with the driven frequency t_Ω and double-periodic resonances disappear.

The edge nodes on the left side of the row with the order $m = 2$ (named as site 1) is inspired by the signal with constant amplitude 1. Under the coexistence of the zero and π mode, the response signals at site 1 are calculated as the red lines in Fig. 4a. By contrast, the equivalent time-modulation signal with the driven frequency t_Ω and the response signal at the bulk site (indicated as site 2 at the right side of the site 1 on the first row) are formed and calculated as the black-dash and blue lines. Comparing with the period of the driven frequency $T = \frac{2\pi}{t_\Omega}$, the results illustrate that the double-periodic resonance emerges at the edge node. Furtherly, the time-modulation and the response signals at site 1 are Fourier transformed as the black-dash and red lines in Fig. 4c. The results show that the edge signal at site 1 possesses the half-frequency resonance at $\frac{t_\Omega}{2}$. When the values of the intralayer-coupling capacitors $C_{a/b}$ are exchanged, the model only possess the π mode at the edge nodes. The response signals at sites 1 and 2 showing in Fig. 4b illustrates that the double-periodic resonance disappears. Additionally, the Fourier transform of the response signals furtherly clarifies the non-resonance performance at the edge site as shown in Fig. 4d. The response signals at the edge nodes of the rows of the other orders are also calculated in in the Section 4 in Appendix.

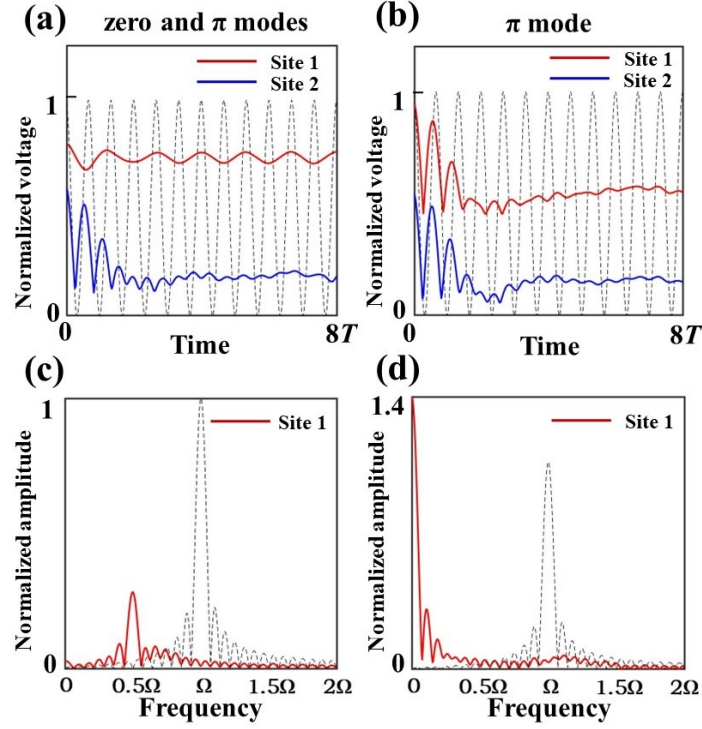


Figure 4. The response signals and “time-periodic-driven” signals on the edge and bulk nodes and the Fourier transform of them. **a**, **b**, the response signals of the edge site (site1 located at the left corner of the row of the order $m = 2$) and bulk site (site 2 locates at right node of site1 on the same row) under the condition of the coexistence of zero and π modes or only the existence of π mode. **c**, **d** the Fourier transformation of the response signals and “driven” signals under the coexistence of zero and π modes or only the existence of π mode. The inspired signal with the constant amplitude 1 is inspired at the site 1. The number of the lattice in each row is 10, and the orders of the rows are $\{m|m \in [-2,2] \text{ and } m \in \mathbb{Z}\}$.

The simulation of the Floquet circuit

From the Fourier-transformation form of the time-dependent Hamiltonian in Eq. 8, the driven frequency is equal to the difference of the on-site energies located on the diagonal position of adjacent rows of the Hamiltonian. In circuit system, the equivalent driven frequency of the Floquet circuit can be gotten from the difference of the resonant frequencies of the grounded- LC resonators on the adjacent rows as $\omega_\Omega = \omega_{0_m} -$

$$\omega_{0_{m-1}} = \frac{1}{\sqrt{L(C_0+mC_\Omega)}} - \frac{1}{\sqrt{L(C_0+(m+1)C_\Omega)}} \text{ which can be equivalent to the difference of the}$$

on-site energies on the adjacent rows. According to the relation $C_\Omega \ll C_0$, the equivalent driven frequency can be expressed as:

$$\begin{aligned}\omega_\Omega = \omega_{0_m} - \omega_{0_{m+1}} &= \frac{1}{\sqrt{L(C_0 + mC_\Omega)}} - \frac{1}{\sqrt{L(C_0 + (m+1)C_\Omega)}} \\ &= \frac{1}{\sqrt{LC_0}} \left(\frac{\sqrt{1 + \frac{(m+1)C_\Omega}{C_0}} - \sqrt{1 + \frac{mC_\Omega}{C_0}}}{\sqrt{1 + \frac{mC_\Omega}{C_0}} \sqrt{1 + \frac{(m+1)C_\Omega}{C_0}}} \right)\end{aligned}\quad (13)$$

where m represents the number of the m th row. We use Taylor series to simplified the numerator in parentheses and the denominator is near to 1:

$$\begin{aligned}\sqrt{1 + \frac{mC_\Omega}{C_0}} &= 1 + \frac{1}{2} \frac{mC_\Omega}{C_0} + o\left(\frac{mC_\Omega}{C_0}\right), \\ \sqrt{1 + \frac{(m+1)C_\Omega}{C_0}} &= 1 + \frac{1}{2} \frac{(m+1)C_\Omega}{C_0} + o\left(\frac{(m+1)C_\Omega}{C_0}\right)\end{aligned}\quad (14)$$

where $o(x)$ represents the infinitesimal when x is close to zero. we substitute Eq. 14 into Eq. 13:

$$\omega_\Omega = \omega_{0_m} - \omega_{0_{m+1}} \approx \frac{1}{\sqrt{LC_0}} \left(\frac{C_\Omega}{2C_0} \right)\quad (15)$$

which presents that the equivalent driven frequencies on different locations of the adjacent rows are approximate equality under the condition of $C_\Omega \ll C_0$.

Here the Floquet circuit is constructed in the software of PathWave and simulating the Floquet-topological bulk-boundary correspondence in the circuit. The source is set as the constant-current amplitude $1 A$ in the Frequency domain and added on the site 1, and the results is shown in Fig. 5a, b. The voltage peak at the frequency 503.080 KHz located in the intra-layer band gap 503.055 – 503.096 KHz as Fig. 5a is the frequency of the zero mode. The difference of the edge and bulk voltages is very large because the loss of the circuit elements is not considered here. Thus, the expression of the voltage amplitude is presented by using the logarithmic formation. The voltage distribution of the zero mode is shown as Fig. 5c. Analogously, the peak at 503.113 KHz located in the inter-layer band gap 503.108 – 503.119 KHz in Fig. 5b is the frequency of the π mode, and the voltage-spatial distribution is shown in Fig. 5d. The zero- and π -mode spatial distributions at the circuit nodes presents the topological boundary-bulk correspondence. Then, the step signal with $0 A$ when the time is less

than $1 \mu\text{s}$ and $1 A$ when the time is higher than $1 \mu\text{s}$ is added on the site 1. The response voltage on site 1 in time domain is shown as Fig. 5e. The results present that the voltage possesses a high-resonant frequency as $\omega_H = \frac{1}{\sqrt{L(C_0+2C_\Omega)}} = 503 \text{ KHz}$, and a low-frequency fluctuation with $\omega_L = \omega_\pi^{(2)} - \omega_0^{(2)} = 33 \text{ Hz}$. We substitute the values of the elements into Eq. 15 and get the driven frequency and period as 65.43 Hz and 15.29 ms . The edge signal in Fig. 5e is Fourier transformed under the frequency from 0 to 100 Hz , and the results is shown in Fig. 5f. From the results of the circuit simulation in Fig. 5e and 5f, the period and frequency of the subharmonic oscillation is 32.87 ms and 32.1 Hz , which is approximately double-driven period of the driven frequency. The simulation results show that the topological π mode and the subharmonic oscillation can be excited at the edge nodes in the Floquet circuit.

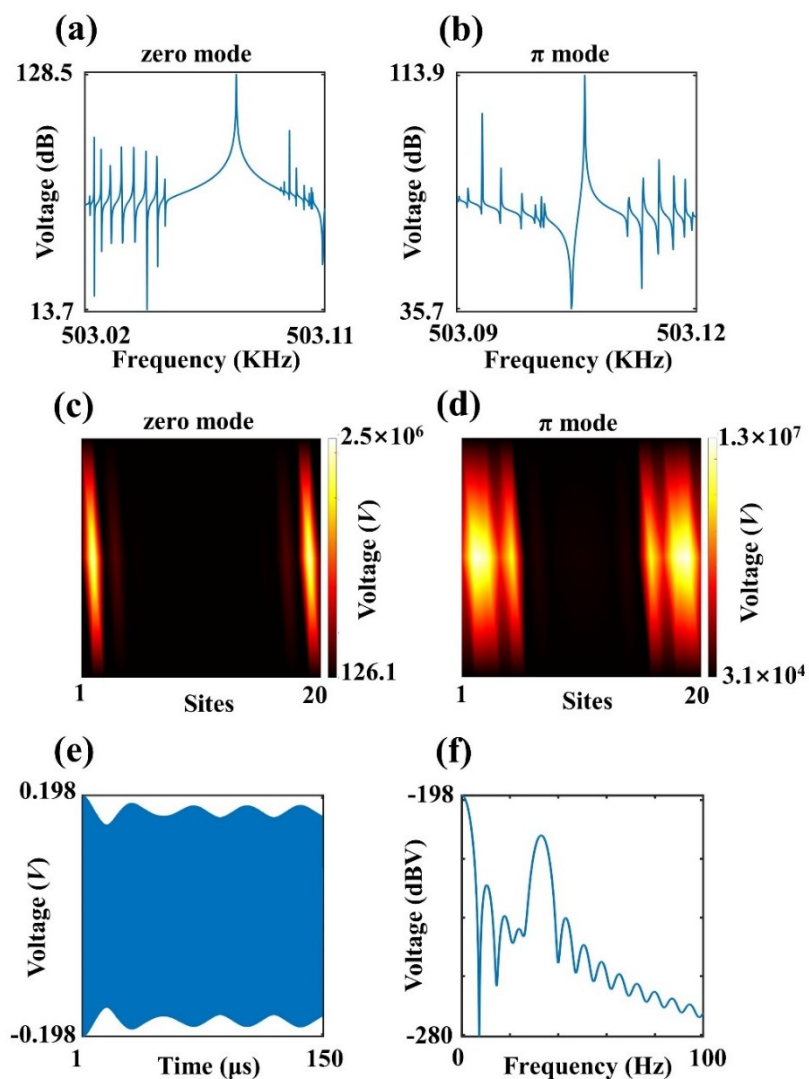


Figure 5. The simulation results of the Floquet circuit under the coexistence of zero and π modes. **a, b**, the voltages in frequency domain with the excited-current signal is added at site 1. **c, d**, the spatial distribution of the zero and π modes at the row of the order $m = 2$. **e**, the response voltages in time domain at the edge and bulk sites. The excited signal is set as the step signal that presents 0 A with the time less than 1 μs and 1 A when the time over 1 μs . **f**, the Fourier transformation of the response signals on the edge site at the frequencies 0 to 100 Hz.

Conclusion

In this paper, we propose a Floquet topological circuit to achieve the Floquet topological phase by constructing the frequency-synthetic dimension. The Floquet π mode and deeply subharmonic oscillation are researched in the circuit system. The Floquet band of the circuit with large time-modulation amplitude is also investigated. In the future, utilized the flexibility of the circuit, we can construct the non-Hermitian or non-linear floquet topological system based on the frequency-synthetic dimension.

Acknowledgements

B.L. was sponsored by the National Natural Science Foundation of China under Grant No. 61901133. J.S. was sponsored by National Natural Science Foundation of China (NSFC) (62275061, 62175049, U22A2014); Natural Science Foundation of Heilongjiang Province in China (ZD2020F002); 111 project to the Harbin Engineering University (B13015); Fundamental Research Funds for the Central Universities (3072022TS2509). F. M. was sponsored by National Natural Science Foundation of China (NSFC) under Grant No. U22A2014.

Data availability

The data that support the findings of this study are available from the corresponding author upon reasonable request.

AUTHOR CONTRIBUTIONS

B. L. conceived the idea. B. L., S. X., Y. T., T. L., H. M., Z. S. and S. W. carried out the calculations of the Floquet bands. B. L., F. M., Z. Z. and J. S. wrote the article. H. T. provides the software PathWave for simulating the circuit. Besides, we are extremely grateful to Shunyu Yao at SITP for his help in topological-invariant discussion and Qingqing Cheng at University of Shanghai for Science and Technology for his help in the time-evolution operator calculation.

APPENDIX:

Section 1. The band of the Floquet Hamiltonian with different APM capacitors

Based on the kirchhoff law, we can get the dynamic equations in Fig. 1 in momentum space as

$$\begin{cases} I_{m1} = C_a \frac{d(V_{m1} - V_{m2})}{dt} + C_b \frac{d(V_{m1} - V_{m2} e^{-ik})}{dt} + C_m \frac{dV_{m1}}{dt} + \frac{1}{L_0} \int V_{m1} dt + C_v \frac{d(V_{m1} - V_{m-12})}{dt} + C_v \frac{d(V_{m1} - V_{m-12} e^{-ik})}{dt} + C_v \frac{d(V_{m1} - V_{m+12})}{dt} + C_v \frac{d(V_{m1} - V_{m+12} e^{-ik})}{dt} \\ I_{m2} = C_a \frac{d(V_{m2} - V_{m1})}{dt} + C_b \frac{d(V_{m2} - V_{m1} e^{ik})}{dt} + C_a \frac{dV_{m2}}{dt} + \frac{1}{L_0} \int V_{m2} dt + C_v \frac{d(V_{m2} - V_{m-11})}{dt} + C_v \frac{d(V_{m2} - V_{m-11} e^{ik})}{dt} + C_v \frac{d(V_{m2} - V_{m+11})}{dt} + C_v \frac{d(V_{m2} - V_{m+11} e^{ik})}{dt} \end{cases} \quad (A1)$$

Here we set the total currents on the nodes is zero and differentiate the voltages of the nodes in one-unit cell by the time t and the equations are expressed as

$$\begin{cases} -\frac{V_{m1}}{C_0 L_0} = (1 + t_a + t_b + mt_\Omega) \frac{d^2 V_{m1}}{dt^2} + (-t_a - t_b e^{-ik}) \frac{d^2 V_{m2}}{dt^2} + t_v (1 + e^{-ik}) \frac{d^2 V_{m-12}}{dt^2} + t_v (1 + e^{-ik}) \frac{d^2 V_{m+12}}{dt^2} \\ -\frac{V_{m2}}{C_0 L_0} = (1 + t_a + t_b + mt_\Omega) \frac{d^2 V_{m2}}{dt^2} + (-t_a - t_b e^{ik}) \frac{d^2 V_{m1}}{dt^2} + t_v (1 + e^{ik}) \frac{d^2 V_{m-11}}{dt^2} + t_v (1 + e^{ik}) \frac{d^2 V_{m+11}}{dt^2} \end{cases} \quad (A2)$$

We Substitute $\omega_0^2 = \frac{1}{C_0 L_0}$ the Fourier transform $\frac{d^n f(t)}{dt^n} = (j\omega)^n F(\omega)$ into the

equations and get the forms of the dynamic equations of the circuit as

$$\begin{cases} \frac{\omega_0^2}{\omega^2} V_{m1} = (1 + t_a + t_b + mt_\Omega) V_{m1} + (-t_a - t_b e^{-ik}) V_{m2} + t_v (1 + e^{-ik}) V_{m-12} + t_v (1 + e^{-ik}) V_{m+12} \\ \frac{\omega_0^2}{\omega^2} V_{m2} = (1 + t_a + t_b + mt_\Omega) V_{m2} + (-t_a - t_b e^{ik}) V_{m1} + t_v (1 + e^{ik}) V_{m-11} + t_v (1 + e^{ik}) V_{m+11} \end{cases} \quad (A3)$$

This equation can be simplified as the form as $\frac{\omega_0^2}{\omega^2} V = HV$ and the Hamiltonian of

the circuit has the forms as the Eq. 6.

The Floquet spectrum of the Hamiltonian in Eq. 10 under the condition of the

different APM capacitor t_v is calculated as the Fig. 6. When the APM capacitors is set as 10 pF which is much less than the intralayer-coupling capacitors t_a/t_b , the hopping terms $H_{\pm 1}$ can be regard as the very small perturbation and all the inter-band gaps are almost closed as the Fig. 6a. When the APM capacitor increase as $t_v = t_a$, the inter-band gaps between the bands of the orders $m = \pm 1$ and $m = \pm 2$ (between the green and blue domains) still open, as shown in Fig. 6b. When the APM capacitor increases to the 100 pF, all the inter-band gaps open, as shown in Fig. 6c. If we expect to close the inter-band gaps, we need to increase the value of the DF capacitors. When the APM capacitor increases to 300 pF which is higher than the intra-layer capacitors, the bands of adjacent orders have some coincident eigenvalues with different k , which leads the circuit has the intra-layer gaps only in the band of the order $m = 0$, as shown in Fig. 6d. When the APM capacitor increase to 1 nF, the intralayer bands of each order gradually getting closer, as shown in Fig. 6e. At last, the APM capacitor increases to 1 μ F, all the intralayer bands of each order are complete overlap, and the bands of the order $m = 0$ presents a flat-band form, as shown in Fig. 6f. Here the bands with different orders are indicated as different background colors.

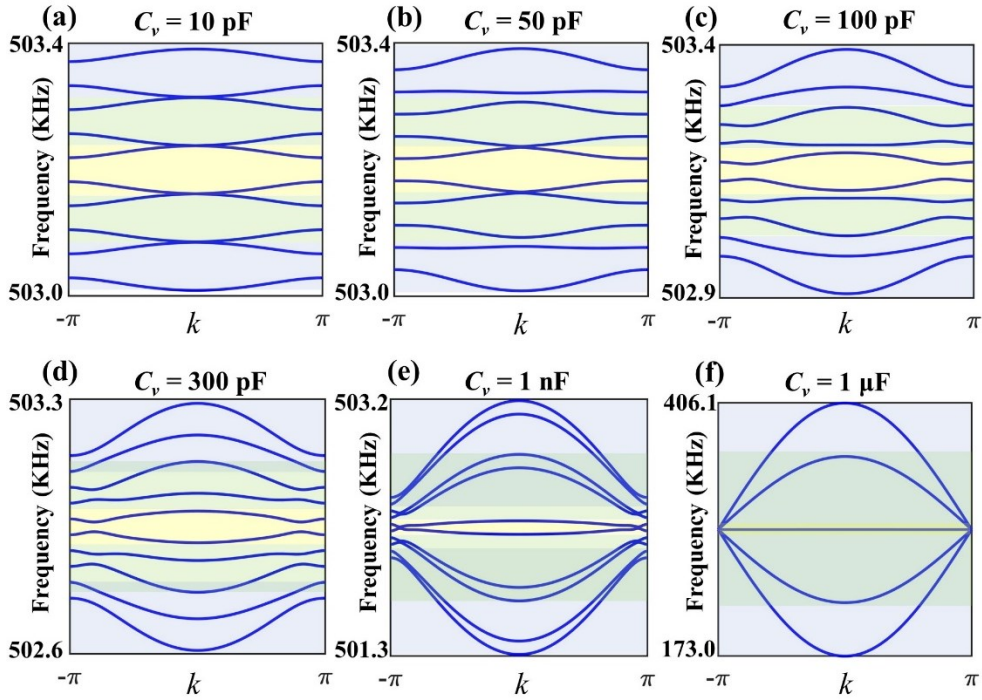


Figure 6. The bands of the Floquet Hamiltonian under different APM capacitors as $C_v = 10$ pF, 50 pF, 100 pF, 300 pF, 1 nF and 1 μ F. The values of other electric elements are

set as $L = 100 \text{ nH}$, $C_0 = 1 \text{ }\mu\text{F}$, $C_a = 100 \text{ pF}$, $C_b = 30 \text{ pF}$ and $C_\Omega = 300 \text{ pF}$. The different-color domains indicate the different orders (the blue/green/yellow domains are corresponding to the order $m = \pm 2/\pm 1/0$).

Section 2. The time-evolution performance of the Hamiltonian

In this section, we research the time-evolution of the Hamiltonian in Eq. 1 and illustrate that the eigen values in the inter-layer gaps are the topological-protected π mode [13].

The time-evolution operator from t_0 to t is expressed as

$$U(t, t_0) = \hat{T} \exp\left(-i \int_{t_0}^t H(t') dt'\right), \quad (\text{A4})$$

where \hat{T} is the time ordering. The time-evolution operator is the solution of the dynamic equation

$$(H(t) - i\partial_t)U(t, t_0) = 0, \quad (\text{A5})$$

Here we define the initial time $t_0 = 0$, and express time-evolution operator as $U(t) = U(t, 0) = \hat{T} \exp\left(-i \int_0^t H(t') dt'\right)$. the effective Hamiltonian is defined as

$$H_{eff} \equiv \frac{i}{T} \ln U(T), \quad (\text{A6})$$

Emphatically, the effective Hamiltonian in this section is different from the effective Hamiltonian of the circuit in the main content. The eigen value of H_{eff} localized in the Floquet Brillouin zone $[-\pi/T, \pi/T]$ is indicated as ε_{eff} , which is shown in Fig. 7a.

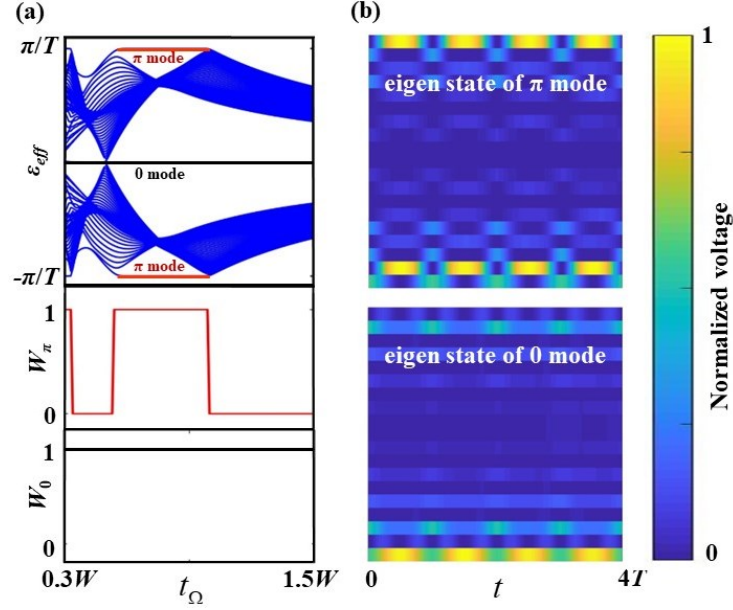


Figure 7. The spectrum of the effective Hamiltonian and the topological performances of the π and zero modes. **a**, the spectrum of the effective Hamiltonian in Floquet Brillouin zone $[-\pi/T, \pi/T]$. The red and black lines indicate the quasienergy of the π and zero modes. The corresponding topological invariants $W_{\pi/0}$ of the π and zero modes are calculated. **b**, the time evolution of the π and zero modes of the circuit with 40 lattice. The main energy of the two topological-protected states is concentrated on the boundaries. The values of the electric elements are set as $L = 100 \text{ nH}$, $C_0 = 1 \text{ }\mu\text{F}$, $C_a = 30 \text{ pF}$, $C_b = 100 \text{ pF}$ and $C_v = 50 \text{ pF}$, and the DF capacitor t_Ω is set in the range of $[0.3W, 1.5W]$.

Here we only discuss the topological performance in the condition of $t_\Omega \geq 0.5W$. Figure 7a shows that the π mode is located at $t_\Omega \in [0.55W, 0.99W]$ and the zero mode always exists at all the t_Ω range. Comparing with the static bandwidth W , the error of the π -mode topological-phase transition point $0.01W$ arises from the effect of the hopping $H_{\pm 1}$ in the second diagonal terms of the Floquet Hamiltonian. Moreover, we investigate the topological properties of the zero and π modes by solving the chiral-gap invariants of the driven model. We define a dimensionless quasienergy $\varepsilon' = \varepsilon_{\text{eff}}T$, which is used to define the branch out of the effective Hamiltonian as

$$H_{eff}^{\varepsilon'} = \frac{i}{T} \ln_{-\varepsilon'} U(T) \quad (\text{A7})$$

Here the complex logarithm $\ln_{\alpha} e^{i\phi}$ with the branch cut satisfies the relation $\ln_{\alpha} e^{i\phi} = i\phi$ for $\alpha - 2\pi < \phi < \alpha$. If we regard the time evolution of the Hamiltonian $H(t)$ as the changes of the phase $\phi(t)$, the logarithm in Eq. A7 indicates that the information of the time evolution is compressed in the range $\varepsilon' - 2\pi < \phi < \varepsilon'$. Obviously, the Hamiltonian H_{eff} in Eq. A3 corresponds to the effective Hamiltonian in Eq. A7 with $\varepsilon' = \pi$. In the follow content in this section, we use the form $H_{eff}^{\varepsilon'}$ for expressing the effective Hamiltonian with branch cut ε' . From the expression Eq. A7, the effective Hamiltonian $H_{eff}^{\varepsilon'}$ cannot be used for solving the topological invariants because it only carries the stroboscopic evolution at integer multiples of T but lacks of the information inside the period. Although the operator $U(t)$ can contain the evolution in the period, it is not periodic $U(t) \neq U(t+T)$. Here we define a periodized evolution operator

$$V_{\varepsilon'}(t) = U(t) \exp(-iH_{eff}^{\varepsilon'} t), \quad (\text{A8})$$

which satisfies the discrete T -translational symmetry $V_{\varepsilon'}(t) = V_{\varepsilon'}(t+T)$ and contains the short-timescale information. Using these features of the operator $V_{\varepsilon'}(t)$, we can construct the relation between the Floquet Hamiltonian H_F and the effective Hamiltonian $H_{eff}^{\varepsilon'}$ as

$$V_{\varepsilon'}^{-1}(t) H_F V_{\varepsilon'}(t) = V_{\varepsilon'}^{-1}(t) (H(t) - \partial_t^2) V_{\varepsilon'}(t) H_{eff}^{\varepsilon'}. \quad (\text{A9})$$

The periodized evolution operator $V_{\varepsilon'}(t)$ is taken as the unitary rotation matrix. This transform relation indicates that the stroboscopic evolution of the time-periodic-driven system can be probed by the Floquet Hamiltonian or the effective Hamiltonian. For the static system, the topological invariant normally comes from the summation over all the bands below the Fermi level. However, for the time-periodic driven system, the Fourier-replica number of the Floquet band is infinite and the strict definition of the Fermi level is nonexistent. Thus, we use the winding number $W_{\varepsilon'}$ defined in chiral

gaps $\varepsilon_{eff} = 0$ or π as the topological invariant in this article. According to the chiral symmetry $\Gamma H(k, t) \Gamma^{-1} = -H(k, -t)$, the periodized evolution operator can be expressed as

$$\Gamma V_{\varepsilon'}(t, k) \Gamma^{-1} = -V_{-\varepsilon'}(-t, k) \exp(2\pi i t / T) \quad (\text{A10})$$

The zero mode corresponds to the branch out $\varepsilon' = 0$. The chiral constraint is expressed as

$$\Gamma V_0\left(\frac{T}{2}, k\right) \Gamma^{-1} = -V_0\left(\frac{T}{2}, k\right), \quad (\text{A11})$$

where the operator presents the antidiagonal form

$$V_0\left(\frac{T}{2}, k\right) = \begin{pmatrix} 0 & V_0^+ \\ V_0^- & 0 \end{pmatrix}. \quad (\text{A12})$$

The winding number for zero mode is solved by

$$W_0 = \frac{i}{2\pi} \int_{-\pi}^{\pi} \text{tr} \left[(V_0^+)^{-1} \partial k V_0^+ \right] dk. \quad (\text{A13})$$

For the π mode corresponding to $\varepsilon' = \pi$, the periodized evolution operator under chiral constraint is the form

$$\Gamma V_{\pi}\left(\frac{T}{2}, k\right) \Gamma^{-1} = V_{\pi}\left(\frac{T}{2}, k\right), \quad (\text{A14})$$

where the operator presents the diagonal form

$$V_{\pi}\left(\frac{T}{2}, k\right) = \begin{pmatrix} V_{\pi}^+ & 0 \\ 0 & V_{\pi}^- \end{pmatrix}. \quad (\text{A15})$$

The winding number for π mode is calculated by

$$W_{\pi} = \frac{i}{2\pi} \int_{-\pi}^{\pi} \text{tr} \left[(V_{\pi}^+)^{-1} \partial k V_{\pi}^+ \right] dk. \quad (\text{A16})$$

The winding number W_{π} and W_0 with different driven frequencies is shown in Fig. 7a. For the π mode, the nontrivial topological-protected states emerge with the condition of $t_{\Omega} \in [0.55W, 0.99W]$ which corresponds to the Winding number $W_{\pi} = 1$. The process of the topological alteration indicated by Winding number further illustrate the phase transition in π gap of the spectrum of H_{eff} . Resembling to the π mode, the topological feature of zero mode indicated by Winding number which reads $W_0 = 1$ also

conforms to the nontrivial-topological features in zero gap.

Then, the time evolution of the π and zero modes is calculated in Fig. 7b. The energy of the nontrivial modes mainly distributes at the edge nodes. The dynamic frequencies of π and zero modes is equal to the driven frequency. This energy-spatial distribution illustrates the topological bulk-boundary correspondence. In the subsequent content, the subharmonic oscillation will be observed at the edge nodes in the condition of the coexist of π and zero modes.

Section 3. The dynamics of the circuit with only zero modes

Here we investigate the topological edge states of the circuit with only zero modes. Then we set the intralayer capacitors as $t_a < t_b$ and the driven capacitors as $t_\Omega > W$. Under this condition, the system only own the zero modes. The spectrum and voltage distribute of the zero modes are calculated as Fig. 9a and Fig. 9b. The results show that the states of the zero modes presents the edge-bulk correspondence at each row of the circuit.

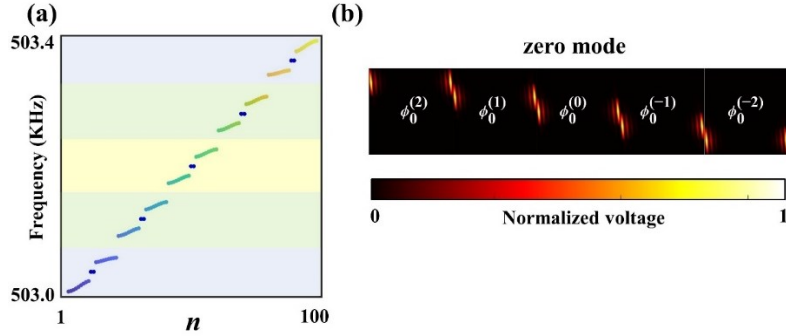


Figure 8. The spectrum under the existence of only the zero mode and the spatial distribution of the zero-mode states. **a**, the spectrum of the Floquet Hamiltonian with open boundary and the number of the lattice is 10. The blue points in the intra-band gaps are the eigen values of zero modes. **b**, the voltage distribution of the zero-modes states. The labels $\phi_0^{(m)}$ indicate the zero-mode eigen states at the intra-band gap of the band of the order m .

The topological performance of the zero and π modes in circuit-SSH model is related with the values of the $t_{a/b}$, t_Ω and W . The topological invariant of the two

modes is calculated as the Eq. A13 and Eq. A16 in Appendix Section 2. When the topological performance of the zero and π modes are nontrivial or trivial, the edge states of the circuit are shown as the Fig. 9, which shows that the topological edge-bulk correspondence is merged with the nontrivial topological performance.

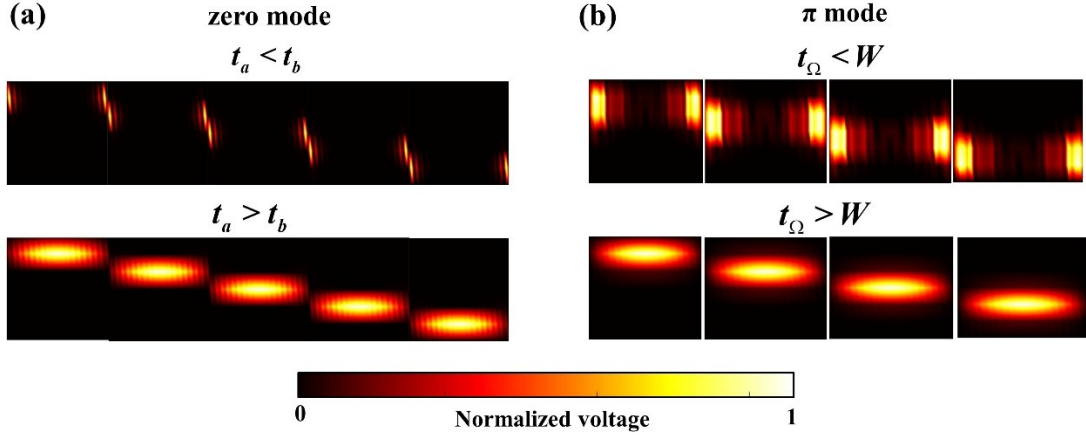


Figure 9. The spatial distribution of the states with nontrivial and trivial states of (a) zero and (b) π modes in the Floquet circuit. The number of the lattice and rows are 10 and 5.

Section 4. The response signals on the edge nodes

The response signals at the edge nodes of different rows. Under the condition of coexistence of zero and π modes, the double-periodic resonances at the edge nodes of the 1st to 5th rows are presented in Fig. 10a. When the values of the intra-layer coupling capacitor are exchanged, the response signals on the edge nodes of different rows are presented in Fig. 10b. All the double-periodic resonances disappear and some resonances with the “driven frequency” as the DF capacitor t_Ω arise at the edge nodes of the 2nd to 4th rows.

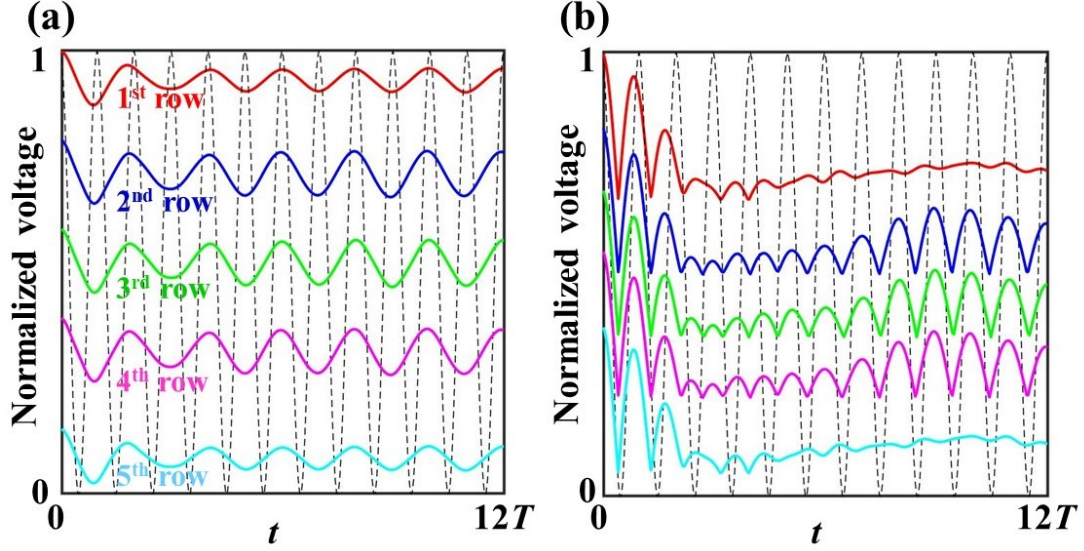


Figure 10. The response signals on the edge nodes of different rows. **a**, the response signals on the edge nodes under the condition of the coexistence of zero and π modes. The red/blue/green/ purple/ cyan lines indicate the response signals on the edge nodes of the 1st/2nd/3rd/4th/5th rows, which correspond to the $m = 2/1/0/-1/-2$ orders. The response signals on the edges under the condition of the only existence of π modes. The Correspondence of the color of the lines and the orders are the same as **a**. The dashed line indicates the signal with the driven frequency equaled to the DF capacitor t_{Ω} .

Reference

- [1] M. Z. Hasan and C. L. Kane, *Colloquium: Topological insulators*, Rev. Mod. Phys 82, 3045 (2010).
- [2] J. E. Moore, *The birth of topological insulators*, Nature 464, 194 (2010).
- [3] Y. Tokura, K. Yasuda and A. Tsukazaki, *Magnetic topological insulators*, Nat Rev Phys 1, 126 (2019).
- [4] L. Fu, C. L. Kane and E. J. Mele, *Topological Insulators in Three Dimensions*, Phys. Rev. Lett 98, 106803 (2007).
- [5] W. –L. Qi and S. –C. Zhang, *Topological insulators and superconductors*, Rev. Mod. Phys 83, 1057 (2011).
- [6] M. C. Rechtsman, J. M. Zeuner, Y. Plotnik, Y. Lumer, D. Podolsky, F. Dreisow, S. Nolte, M. Segev and A. Szameit, *Photonic Floquet topological insulators*, Nature 496,

196 (2013).

[7] M. S. Rudner and N. H. Lindner, Band structure engineering and non-equilibrium dynamics in Floquet topological insulators, *Nat Rev Phys* 2, 229 (2020).

[8] R. Roy and F. Harper, Periodic table for Floquet topological insulators, *Phys. Rev. B* 96, 155118 (2017).

[9] S. K. Ivanov, Y. Zhang, Y. V. Kartashov and D. V. Skryabin, Floquet topological insulator laser, *APL Photonics* 4, 126101 (2019).

[10] S. Yao, Z. Yan and Z. Wang, Topological invariants of Floquet systems: General formulation, special properties, and Floquet topological defects, *Phys. Rev. B* 96, 195303 (2017).

[11] Q. Cheng, Y. Pan, H. Wang, C. Zhang, D. Yu, A. Gover, H. Zhang, T. Li, L. Zhou, and S. Zhu, Observation of Anomalous π Modes in Photonic Floquet Engineering, *Phys. Rev. Lett.* 122, 173901 (2019).

[12] S. Wu, W. Song, S. Gao, Y. Chen, S. Zhu and T. Li, Floquet π mode engineering in non-Hermitian waveguide lattices, *Phys. Rev. Research* 3, 023211 (2021).

[13] Y. Pan and B. Wang, Time-crystalline phases and period-doubling oscillations in one-dimensional Floquet topological insulators, *Phys. Rev. Research* 2, 043239 (2020).

[14] B. Wang, J. Quan, J. Han, X. Shen, H. Wu and Y. Pan, Observation of Photonic Topological Floquet Time Crystals, *LASER PHOTONICS REV* Ipor. 202100469 (2022).

[15] L. Jiang, T. Kitagawa, J. Alicea, A. R. Akhmerov, D. Pekker, G. Refael, J. I. Cirac, E. Demler, M. D. Lukin, and P. Zoller, Majorana Fermions in Equilibrium and in Driven Cold-Atom Quantum Wires, *Phys. Rev. Lett.* 106, 220402 (2011).

[16] M. Thakurathi, A. A. Patel, D. Sen, and A. Dutta, Floquet generation of Majorana end modes and topological invariants, *Phys. Rev. B* 88, 155133 (2013).

[17] A. Kundu and B. Seradjeh, Transport Signatures of Floquet Majorana Fermions in Driven Topological Superconductors, *Phys. Rev. Lett.* 111, 136402 (2013).

[18] P. Mognini, Wei Chen, and R. Chitra, Universal quantum criticality in static and Floquet-Majorana chains, *Phys. Rev. B* 98, 125129 (2018).

[19] X. Zhang and J. Gong, Non-Hermitian Floquet topological phases: Exceptional

- points, coalescent edge modes, and the skin effect, *Phys. Rev. B* 101, 045415 (2020).
- [20] H. Dehghani, T. Oka and A. Mitra, Out-of-equilibrium electrons and the Hall conductance of a Floquet topological insulator, *Phys. Rev. B* 91, 155422 (2015).
- [21] K. W. Kim, D. Bagrets, T. Micklitz and A. Altland, Quantum Hall criticality in Floquet topological insulators, *Phys. Rev. B* 101, 165401 (2020).
- [22] H. Wang, L. Zhou, and Y. D. Chong, Floquet Weyl phases in a three-dimensional network model, *Phys. Rev. B* 93, 144114 (2016).
- [23] L. Bucciantini, S. Roy, S. Kitamura and T. Oka, Emergent Weyl nodes and Fermi arcs in a Floquet Weyl semimetal, *Phys. Rev. B* 96, 041126(R) (2017).
- [24] H. Hübener, M. A. Sentef, U. D. Giovannini, A. F. Kemper and A. Rubio, Creating stable Floquet–Weyl semimetals by laser-driving of 3D Dirac materials, *Nat. Commun* 8, 13940 (2017).
- [25] Z. Yan and Z. Wang, Floquet multi-Weyl points in crossing-nodal-line semimetals, *Phys. Rev. B* 96, 041206(R) (2017).
- [26] R. Chen, D.-H. Xu, and B. Zhou, Floquet topological insulator phase in a Weyl semimetal thin film with disorder, *Phys. Rev. B* 98, 235159 (2018).
- [27] M. Umer, R. W. Bomantara, and J. Gong, Dynamical characterization of Weyl nodes in Floquet Weyl semimetal phases, *Phys. Rev. B* 103, 094309 (2021).
- [28] S. Franca, J. van den Brink and I. C. Fulga, An anomalous higher-order topological insulator, *Phys. Rev. B* 98, 201114(R) (2018).
- [29] M. R. -Vega, A. Kumar and B. Seradjeh, Higher-order Floquet topological phases with corner and bulk bound states, *Phys. Rev. B* 100, 085138 (2019).
- [30] T. Nag, V. Juričić, and B. Roy, Out of equilibrium higher-order topological insulator: Floquet engineering and quench dynamics, *Phys. Rev. Research* 1, 032045(R) (2019).
- [31] Y. Peng, Floquet higher-order topological insulators and superconductors with space-time symmetries, *Phys. Rev. Research* 2, 013124 (2020).
- [32] B. Huang and W. V. Liu, Floquet Higher-Order Topological Insulators with Anomalous Dynamical Polarization, *Phys. Rev. Lett.* 124, 216601 (2020).
- [33] H. Hu, B. Huang, E. Zhao, and W. V. Liu, Dynamical Singularities of Floquet

- Higher-Order Topological Insulators, *Phys. Rev. Lett.* 124, 057001 (2020).
- [34] D. Vu, R. -X. Zhang, Z. -C. Yang and S. D. Sarma, Superconductors with anomalous Floquet higher-order topology, *Phys. Rev. B* 104, L140502 (2021).
- [35] T. Nag, V. Juričić and Bitan Roy, Hierarchy of higher-order Floquet topological phases in three dimensions, *Phys. Rev. B* 103, 115308 (2021).
- [36] W. Zhu, Y. D. Chong and J. Gong, Floquet higher-order topological insulator in a periodically driven bipartite lattice, *Phys. Rev. B* 103, L041402 (2021).
- [37] W. Zhu, H. Xue, J. Gong, Y. Chong and B. Zhang, Time-periodic corner states from Floquet higher-order topology, *Nat. Commun* 13, 11 (2022).
- [38] M. D. Reichl and E. J. Mueller, Floquet edge states with ultracold atoms, *Phys. Rev. A* 89, 063628 (2014).
- [39] Karen Wintersperger, Christoph Braun, F. Nur Ünal, André Eckardt, Marco Di Liberto, Nathan Goldman, Immanuel Bloch & Monika Aidelsburger Realization of an anomalous Floquet topological system with ultracold atoms. *Nat. Phys.* 16, 1058 (2020).
- [40] P. Wang, Q. -F. Sun and X. C. Xie, Transport properties of Floquet topological superconductors at the transition from the topological phase to the Anderson localized phase, *Phys. Rev. B* 90, 155407 (2014).
- [41] Y. Peng and G. Refael, Time-quasiperiodic topological superconductors with Majorana multiplexing, *Phys. Rev. B* 98, 220509(R) (2018).
- [42] T. Čadež, R. Mondaini and P. D. Sacramento, Edge and bulk localization of Floquet topological superconductors, *Phys. Rev. B* 99, 014301 (2019).
- [43] T. Čadež, R. Mondaini and P. D. Sacramento, Edge and bulk localization of Floquet topological superconductors, *Phys. Rev. B* 99, 014301 (2019).
- [44] K. Plekhanov, M. Thakurathi, D. Loss and J. Klinovaja, Floquet second-order topological superconductor driven via ferromagnetic resonance, *Phys. Rev. Research* 1, 032013(R) (2019).
- [45] L. Zhou, Non-Hermitian Floquet topological superconductors with multiple Majorana edge modes, *Phys. Rev. B* 101, 014306 (2020).
- [46] A. K. Ghosh, T. Nag, and A. Saha, Floquet generation of a second-order topological superconductor, *Phys. Rev. B* 103, 045424 (2021).

- [47] A. K. Ghosh, T. Nag, and A. Saha, Floquet second order topological superconductor based on unconventional pairing, *Phys. Rev. B* 103, 085413 (2021).
- [48] R. -X. Zhang and S. D. Sarma, Anomalous Floquet Chiral Topological Superconductivity in a Topological Insulator Sandwich Structure, *Phys. Rev. Lett.* 127, 067001 (2021).
- [49] H. Dehghani, M. Hafezi and P. Ghaemi, Light-induced topological superconductivity via Floquet interaction engineering, *Phys. Rev. Research* 3, 023039 (2021).
- [50] S. Kitamura and H. Aoki, Floquet topological superconductivity induced by chiral many-body interaction, *Commun Phys* 5, 174 (2022).
- [51] R. Ge, W. Broer and T. C. H. Liew, Floquet topological polaritons in semiconductor microcavities, *Phys. Rev. B* 97, 195305 (2018).
- [52] W. Zheng and H. Zhai, Floquet topological states in shaking optical lattices, *Phys. Rev. A* 89, 061603(R) (2014).
- [53] S. Choudhury and E. J. Mueller, Stability of a Floquet Bose-Einstein condensate in a one-dimensional optical lattice, *Phys. Rev. A* 90, 013621 – Published 21 July 2014.
- [54] T. A. Sedrakyan, V. M. Galitski and A. Kamenev, Statistical Transmutation in Floquet Driven Optical Lattices, *Phys. Rev. Lett.* 115, 195301 (2015).
- [55] C. Sträter, S. C.L. Srivastava and André Eckardt, Floquet Realization and Signatures of One-Dimensional Anyons in an Optical Lattice, *Phys. Rev. Lett.* 117, 205303 (2016).
- [56] J. -Y. Shan, M. Ye, H. Chu, S. Lee, J. -G. Park, L. Balents and D. Hsieh, Giant modulation of optical nonlinearity by Floquet engineering, *Nature* 600, 235 (2021).
- [57] M. -J. Yin, X. -T. Lu, T. Li, J.-J. Xia, T. Wang, X. -F. Zhang, and H. Chang, Floquet Engineering Hz-Level Rabi Spectra in Shallow Optical Lattice Clock, *Phys. Rev. Lett.* 128, 073603 (2022).
- [58] Y. -G. Peng, C. -Z. Qin, D. -G. Zhao, Y. -X. Shen, X. -Y. Xu, M. Bao, H. Jia and X. -F. Zhu, Experimental demonstration of anomalous Floquet topological insulator for sound, *Nat Commun* 7, 13368 (2016).
- [59] Z. Cheng, R. W. Bomantara, H. Xue, W. Zhu, J. Gong and B. Zhang, Observation

- of $\pi/2$ Modes in an Acoustic Floquet System, *Phys. Rev. Lett.* 129, 254301 (2022).
- [60] S. Imhof, C. Berger, F. Bayer, J. Brehm, L. W. Molenkamp, T. Kiessling, F. Schindler, C. H. Lee, M. Greiter, T. Neupert and R. Thomale, Topoelectrical-circuit realization of topological corner modes, *Nat. Phys.* 14, 925 (2018).
- [61] R. Yu, Y. X. Zhao and A. P. A Schnyder, genuine realization of the spinless 4D topological insulator by electric circuits. *Natl. Sci. Rev.* 7, 1288 (2020).
- [62] W. Zhang, D. Zou, W. He, J. Bao, Q. Pei, H. Sun and X. Zhang, Topoelectrical-circuit realization of 4D hexadecapole insulator. *Phys. Rev. B.* 102, 100102(R) 2020.
- [63] R. Li, B. Lv, H. Tao, J. Shi, Y. Chong, B. Zhang and H. Chen, Ideal type-II Weyl points in topological circuits. *Natl. Sci. Rev.* nwaal92 (2020).
- [64] D. –A. Galeano, X. –X. Zhang, J. Mahecha, Topological circuit of a versatile non-Hermitian quantum system, arXiv: 2204. 01833 (2022).
- [65] S. Weidemann, M. Kremer, S. Longhi, A. Szameit, Topological triple phase transition in non-Hermitian Floquet quasicrystals, *Nature.* 601, 354–359 (2022).
- [66] A. Nagulu, X. Ni, A. Kord, M. Tymchenko, S. Garikapati, A. Alù, H. Krishnaswamy, Chip-scale Floquet topological insulators for 5G wireless systems, *Nat Electron.* 5, 300–309 (2022).
- [67] S. S. Dabiri, H. Cheraghchi, Electric circuit simulation of Floquet topological insulators in Fourier space, *J. Appl. Phys.* 134, 084303 (2023).
- [68] G. Salerno, T. Ozawa, H. M. Price, I. Carusotto, Floquet topological system based on frequency-modulated classical coupled harmonic oscillators. *Phys. Rev. B.* 93, 085105 (2016).
- [69] L. Yuan, Q. Lin, M. Xiao, S. Fan, Synthetic dimension in photonics. *Optica.* 5, 001396 (2018).